The fate of rotating point plumes in unstratified environment: from free growth to boundary interactions

Shuang Wang[1]† and Wanying Kang[1] and Yixiao Zhang[1] and John Marshall[1]

[1]Earth, Atmospheric and Planetary Science Department, Massachusetts Institute of Technology, Cambridge, MA 02139, USA

(Received xx; revised xx; accepted xx)

Plumes generated from a point buoyant source are relevant to hydrothermal vents in lakes and oceans on and beyond Earth. They play a crucial role in determining heat and material transport and thereby local biospheres. In this study, we investigate the development of rotating point plumes in an unstratified environment using both theory and numerical simulations. We find that, in a sufficiently large domain, point plumes cease to rise beyond a penetration height h_f, at which buoyancy flux from the heat source is leaked laterally to the ambient fluid. The height h_f is found to scale with the rotational length scale

$$h_\mathrm{f} \sim L_\mathrm{rot}^p \equiv \left(\frac{F_0}{f^3}\right)^{\frac{1}{4}},$$

where F_0 is the source buoyancy flux and $f = 2\Omega$ is the Coriolis parameter (Ω is the rotation rate). In a limited domain, the plume may reach the top boundary or merge with neighboring plumes. Whether rotational effects dominate depends on how L_rot^p compares to the height of the domain H and the distance between the plumes L. Four parameter regimes can therefore be identified and are explored here through numerical simulation. Our study advances the understanding of hydrothermal plumes and heat/material transport, with applications ranging from subsurface lakes and the oceans in icy worlds such as snowball Earth, Europa, and Enceladus.

Key words: plumes, rotating convection

1. Introduction

Turbulent plumes generated by continuous sources or sinks of buoyancy are ubiquitous in nature. Examples include smoke emitted into the atmosphere from chimneys or volcanic eruptions (e.g., Turner 1973; Baines & Sparks 2005), descending convection in high-latitude oceans or under polynyas caused by surface cooling (e.g., Marshall & Schott 1999; Okada *et al.* 2004), and hot springs in volcanic lakes and oceans both on and beyond Earth (e.g.,

† Email address for correspondence: shuangw@mit.edu

Lupton *et al.* 1985; Varekamp & Rowe 1997; Goodman & Lenferink 2012). Such plumes can affect the spread of pollutants, transport and mixing of heat and materials (e.g., nutrition and biomass), and hence the local environment and biosphere. Understanding the growth and dynamics of such plumes is therefore crucial.

Here, we focus on hydrothermal plumes driven by isolated point sources — also referred to as point plumes — in an unstratified environment. This configuration is less investigated in the context of Earth oceanography, because weakly stratified oceans are less common on Earth as the ocean is predominantly heated from above, and the buoyancy source from the atmosphere is usually associated with large spatial scales (Schott & Leaman 1991; Marshall & Schott 1999). For these reasons, most previous studies of plume convection have focused on penetrative plume in a stratified ocean or convection driven by wide-spread buoyancy sources (see, e.g., Jones & Marshall 1993; Maxworthy 1997; Marshall & Schott 1999). However, the subsurface oceans of icy worlds, for example, snowball Earth (Yang *et al.* 2012; Ashkenazy *et al.* 2013), Europa (the second moon of Jupiter; Goodman *et al.* 2004), and Enceladus (the second moon of Saturn; Kang *et al.* 2022*a*,*b*), are likely not stratified or even convectively unstable due to heat sources on the seafloor. In addition, hydrothermal vent activities have been found to exist on Earth (Thomson *et al.* 1992) and have been hypothesized for icy satellites (Vance & Goodman 2009; Choblet *et al.* 2017), motivating us to investigate the behavior of rotating point plumes in an unstratified fluid (ocean).

Point plumes in an unstratified fluid in the absence of background rotation were first investigated in the milestone study of Morton *et al.* (1956), hereafter referred to as MTT. By hypothesizing that entrainment varies in proportion to the plume velocity, MTT found analytical solutions for the plume characteristics (width, buoyancy, and speed). Such plumes are found to rise in a conical shape with decreasing buoyancy and speed, and have been studied in the laboratory (e.g., Morton *et al.* 1956; Boubnov & van Heijst 1994; Ferrero *et al.* 2022) and numerical experiments (e.g., Abdalla *et al.* 2009; Bhaganagar & Bhimireddy 2020).

In the presence of rotation, a point plume would start life as a nonrotating MTT plume, and then transit to a cylindrical plume with constant buoyancy anomaly surrounded by rim currents. The transition height and the width of the plume follow the rotational length scale $L^p_{\mathrm{rot}} \equiv (F_0/f^3)^{1/4}$, the only length scale in the system independent of diffusivity or viscosity. Here, F_0 is the buoyancy at the source, and f is the Coriolis parameter. This is supported by laboratory experiments (Fernando *et al.* 1998; Goodman *et al.* 2004; Ferrero *et al.* 2022) and numerical simulations (Goodman & Lenferink 2012). Upon impact of an upper boundary, cylindrical plumes are found to undergo baroclinic instability, scattering buoyancy away from the source (Fernando *et al.* 1998; Goodman *et al.* 2004).

However, a rotating plume does not necessarily reach the top surface in an unstratified environment. Water tank experiments by Goodman *et al.* (2004) and oceanic numerical simulations by Kang *et al.* (2022*a*) and Bire *et al.* (2023) demonstrate that concentrated plumes can break up into eddies in the mid-tank/ocean, indicating that the rotation-dominated cylindrical plume may not be the final stage of their evolution. This final stage has rarely been investigated, despite its critical role in determining whether heat and tracers remain concentrated during transport to the surface.

In this paper, we investigate the development of rotating point plumes in an unstratified fluid using both theoretical analysis and numerical simulations. We aim to address two key questions: (1) What factors determine whether a plume remains concentrated as it approaches the top surface or instead disperses before doing so? (2) How does a plume evolve after impacting boundaries? Our paper is organized as follows. A brief description of our numerical method is provided in § 2. The development of a free point plume unconstrained by boundaries is presented in § 3, followed by the development of the plume in a finite domain

(§ 4). The effect of source size is discussed in § 5, and key conclusions are summarized in § 6.

2. Numerical method

2.1. *Key parameters*

The plume is driven by a buoyancy source at the bottom and grows in a rectangular domain that rotates along the $z-$axis at rate Ω. Thus, our system has five free parameters $(L,\ H,\ r_s,\ F_0,\ f)$, where L and H are the width and height of the domain, r_s is the radius of the source as the "point" source is actually a finite circular area, F_0 (with units of $\mathrm{m}^4\ \mathrm{s}^{-3}$) is the buoyancy flux imposed at the source, and $f = 2\Omega$ is the Coriolis parameter.

The dynamics of the rotating point plumes, where the source size r_s is small enough to be approximated as a geometric point, are primarily governed by F_0 and f. These two physical parameters define a length scale,

$$L_{\mathrm{rot}}^{p} = \left(\frac{F_0}{f^3}\right)^{\frac{1}{4}}, \tag{2.1}$$

where the superscript 'p' indicates a point plume. This rotational length scale has been extensively used to describe the characteristic scale of convective plumes in a rotating regime, such as Speer & Marshall (1995), Fernando *et al.* (1998), and Bire *et al.* (2023).

Naturally, the system can be nondimensionlized using L_{rot}^{p}, yielding the dimensionless parameters

$$\left(\widehat{L},\ \widehat{H},\ \widehat{r}_s\right) \equiv \left(\frac{L}{L_{\mathrm{rot}}^{p}},\ \frac{H}{L_{\mathrm{rot}}^{p}},\ \frac{r_s}{L_{\mathrm{rot}}^{p}}\right). \tag{2.2}$$

Hereafter, $\widehat{(\cdot)}$ denotes dimensionless parameters. The point source corresponds to $\widehat{r}_s \ll 1$, so its geometry is negligible. Instead of using $\widehat{L}$ and $\widehat{H}$, the following two dimensionless numbers are more commonly used and more convenient for analyses:

$$(\Gamma,\ Ro^{*p}) \equiv \left(\frac{L}{H},\ \frac{L_{\mathrm{rot}}^{p}}{H}\right), \tag{2.3}$$

where Γ is the domain aspect ratio, and Ro^{*p} is the natural Rossby number for rotating point plumes that describes the extent to which rotation dominates the dynamics when the plume reaches the surface at height H (Goodman *et al.* 2004; Goodman & Lenferink 2012; Bire *et al.* 2023).

When the source size is non-negligible, i.e. $\widehat{r}_s \gtrsim 1$, the buoyancy flux per unit area should be the key parameter determining plume dynamics. In this circumstance, the rotational length scale can be formulated as

$$L_{\mathrm{rot}}^{a} = \left(\frac{F_0}{r_s^2 f^3}\right)^{\frac{1}{2}}, \tag{2.4}$$

where the superscript 'a' represents per unit area. This L_{rot}^{a} has been commonly used in studies of convection driven by wide and homogeneous buoyancy sources (e.g., Stone 1968; Fernando *et al.* 1991; Bire *et al.* 2022).

In § 3 and § 4, we focus on the former case, where the buoyancy source can be treated as a geometric point, and the influence of the source radius on the plume dynamics is explored further in § 5.

2.2. *Experimental design*

We perform high-resolution simulations for rotating hydrothermal plumes using *Oceananigans.jl*, a GPU-based general circulation model (GCM) written in Julia language with extraordinary computational performance (Ramadhan *et al.* 2020). Our domain spans from $-L/2$ to $L/2$ in both $x-$ and $y-$directions with doubly periodic boundary conditions. In the vertical direction ($z-$direction), our domain covers $z = 0$ to $z = H$. The rotation rate is set to Ω along the $z-$axis. The initial velocity and buoyancy are both set to zero.

At the bottom $z = 0$, a steady, axis-symmetric, Gaussian-like buoyancy flux is prescribed:

$$F(x, y) = F_A \exp\left(-\frac{x^2 + y^2}{r_s^2}\right), \tag{2.5}$$

where F_A is the maximum buoyancy flux per unit area. The total buoyancy flux is thus given by

$$F_0 = \iint F(x, y)\mathrm{d}x\mathrm{d}y = \pi r_s^2 F_A. \tag{2.6}$$

In this rotating-plume system, two types of instabilities play a role in the plume development. The first is the Kelvin–Helmholtz instability (hereafter KHI), which occurs during the initial stage, and it triggers the transition from a laminar state to a turbulent state. The second instability is baroclinic instability (hereafter BCI), which occurs after the plume fully develops. It drives lateral mixing between the plume and the ambient fluid. Capturing both instabilities is challenging as BCI occurs at much larger length scales than KHI. To proceed, we set a non-uniform mesh that is refined near the source and gradually coarsens in the upper domain. The dimensionless horizontal and vertical grid sizes, $\widehat{\Delta}_h$ and $\widehat{\Delta}_z$, are given by

$$\widehat{\Delta}_h \equiv \frac{\Delta_h}{L^p_{\mathrm{rot}}} = 0.04, \quad \widehat{\Delta}_z \equiv \frac{\Delta_z}{L^p_{\mathrm{rot}}} = \begin{cases} 0.02 & 1 \leqslant N_z \leqslant 300, \\ 0.02 \times 1.01^{(N_z-300)} & 301 \leqslant N_z \leqslant 450, \\ 0.02 \times 1.01^{150} & 451 \leqslant N_z \leqslant 1050, \end{cases}$$

where N_z denotes the vertical grid index, and subscripts 'h' and 'z' refer to horizontal and vertical directions, respectively. The total number of grid cells is 486 in both directions $x-$ and $y-$ and is 1050 in the vertical, resulting in a dimensionless domain size of $\widehat{L} = 19.44$ and $\widehat{H} = 66.34$. One experiment using this refined mesh is conducted as the reference case, which is referred to as *Exp-refined* (table 1). The results of this experiment are presented in figure 1. However, due to computational resource limitations, most experiments are performed on a uniform mesh with somewhat lower resolution (the series labeled *Exp-free* and *Exp-res* in table 1). The reduced resolution may delay the onset of KHI due to a compromised ability to resolve small-scale turbulence, potentially affecting the subsequent onset of BCI and our main results. To assess the numerical convergence with respect to resolution, a grid sensitivity analysis is presented in § 3.4.

To monitor the development of plumes, we define the envelope of the plume as the isosurface of $b/b_{\mathrm{max}} = 0.1\%$, where b_{max} is the buoyancy at the source. To diagnose the height of the plume, we use the highest height of the $\overline{b}^y/\overline{b}^y_{\mathrm{max}} = 0.1\%$ isoline, where $\overline{b}^y$ is the buoyancy averaged along the $y-$direction. This approach, equivalent to a side-view perspective, minimizes the need to store large three-dimensional datasets and ensures that the highest plume front is captured regardless of its position.

3. Development of a free single point plume

We begin by investigating the development of a single free plume, unaffected by any boundaries. Initially, it behaves like a free-turbulent plume. As rotation becomes significant, it transforms into a Taylor column and eventually becomes destabilized (figure 1).

In this section, we conduct the numerical experiments listed in the upper part of table 1. The results used to visualize the plume evolution are taken from *Exp-refined*. Other experiments were performed on a lower resolution uniform mesh. The sensitivity of our results to grid resolution is examined in § 3.4.

3.1. *Stage-1: free-turbulent plume*

In the first stage, the buoyant fluid emanating from the source is not yet influenced by rotation, so the plume is filled by three-dimensional turbulence. These turbulent motions entrain dense ambient fluid into the plume, reducing its buoyancy and vertical velocity while expanding laterally to form a cone shape (stage-1 in figure 1*a*).

During this stage, F_0 is the only external dimension parameter that determines the plume. As shown in MTT, the radius of the plume R, the upwelling velocity W, and buoyancy anomaly B at the plume center follow,

$$R(z) = \frac{6}{5}\alpha z \approx 0.11z, \tag{3.1}$$

$$W(z) = \frac{5}{6\alpha}\left[\frac{9\alpha}{5}\left(\frac{2F_0}{\pi}\right)\right]^{\frac{1}{3}} z^{-\frac{1}{3}} \approx 4.25\left(F_0 z^{-1}\right)^{\frac{1}{3}}, \tag{3.2}$$

$$B(z) = \frac{5}{6\alpha}\left[\frac{9\alpha}{5}\left(\frac{2F_0}{\pi}\right)\right]^{-\frac{1}{3}}\left(\frac{2F_0}{\pi}\right) z^{-\frac{5}{3}} \approx 12\left(F_0^2 z^{-5}\right)^{\frac{1}{3}}, \tag{3.3}$$

where α is the entrainment coefficient (= 0.093 for buoyant plume; Morton *et al.* 1956). Also, we can obtain a volume flux μ and a momentum flux m from MTT,

$$\mu(z) = \frac{6\alpha\pi}{5}\left[\frac{9\alpha}{5}\left(\frac{2F_0}{\pi}\right)\right]^{\frac{1}{3}} z^{\frac{5}{3}} \approx 0.17\left(F_0 z^5\right)^{\frac{1}{3}}, \tag{3.4}$$

$$m(z) = \frac{\pi}{2}\left[\frac{9\alpha}{5}\left(\frac{2F_0}{\pi}\right)\right]^{\frac{2}{3}} z^{\frac{4}{3}} \approx 0.35(F_0 z^2)^{\frac{2}{3}}, \tag{3.5}$$

which align with the measurements from laboratory experiments (Rouse *et al.* 1952; List & Imberger 1973; List 1982).

The evolution of the plume in the reference case, *Exp-refine*, is shown in figure 1. Within one rotation period after model initialization, a free-turbulent plume is observed. This plume occupies a clearly defined cone shape (figure 1*b*), which aligns with the one predicted by equation (3.1). Figure 1(*h*) shows the vertical profiles of vertical velocity and buoyancy measured along the center of the plume, $W(z)$ and $B(z)$, both of which decrease as the plume rises and align with equations (3.2) and (3.3).

Note that $W(z)$ and $B(z)$ become singular at $z = 0$, indicating that MTT is invalid near the source, as the source cannot be treated as a point there. For a circular source with finite area, the point-plume assumption and the MTT model have been shown to be valid only when $z > 24r_s$ (Fernando *et al.* 1998). In our experiment, the invalid region is highlighted in gray in figure 1(*h*). Within this region, our simulation results indeed depart notably from the MTT prediction. Specifically, $W(z)$ is observed to be zero near the bottom due to boundary effects, whereas the theoretical prediction is infinite.

Exp. name	F_0 ($m^4\,s^{-3}$)	f (s^{-1})	L_{rot}^{p} (m)	$\widehat{L}$	$\widehat{H}$	$\widehat{r}_s$	$\widehat{\Delta}_h$	$\widehat{\Delta}_z$	Γ	Ro^{*p}
Exp-refined	10^{-6}	10^{-6}	1000	19.4	66.3	0.05	0.04	$\geqslant$0.02	0.293	0.015
Exp-free-1	2.56×10^{-10}	10^{-4}	4	50	100	0.05	0.1	0.1	0.5	0.01
Exp-free-2	10^{-8}	10^{-4}	10	50	100	0.05	0.1	0.1	0.5	0.01
Exp-free-3	2.56×10^{-6}	10^{-4}	40	50	100	0.05	0.1	0.1	0.5	0.01
Exp-free-4	10^{-4}	10^{-4}	100	50	100	0.05	0.1	0.1	0.5	0.01
Exp-free-5	2.56×10^{-2}	10^{-4}	400	50	100	0.05	0.1	0.1	0.5	0.01
Exp-free-6	1	10^{-4}	1000	50	100	0.05	0.1	0.1	0.5	0.01
Exp-free-7	10^{-6}	10^{-6}	1000	50	100	0.05	0.1	0.1	0.5	0.01
Exp-free-8	10^{-6}	10^{-6}	1000	25	100	0.05	0.1	0.1	0.25	0.01
Exp-free-9	10^{-6}	10^{-6}	1000	25	200	0.05	0.1	0.1	0.125	0.005
Exp-res-1	10^{-6}	10^{-6}	1000	20	75	0.05	0.05	0.05	0.267	0.013
Exp-res-2	10^{-6}	10^{-6}	1000	50	100	0.05	0.1	0.2	0.5	0.01
Exp-res-3	10^{-6}	10^{-6}	1000	50	100	0.05	0.1	0.25	0.5	0.01
Exp-res-4	10^{-6}	10^{-6}	1000	50	100	0.05	0.1	0.5	0.5	0.01
Exp-res-5	10^{-6}	10^{-6}	1000	50	200	0.05	0.1	1	0.25	0.005
Exp-wall-1	10^{-6}	10^{-6}	1000	0.1	1	0.005	0.001	0.001	0.1	1
Exp-wall-2	10^{-6}	10^{-6}	1000	0.5	5	0.05	0.01	0.01	0.1	0.2
Exp-wall-3	10^{-6}	10^{-6}	1000	1	10	0.05	0.01	0.01	0.1	0.1
Exp-surf-1	10^{-6}	10^{-6}	1000	1	1	0.005	0.002	0.002	1	1
Exp-surf-2	10^{-6}	10^{-6}	1000	5	5	0.05	0.01	0.01	1	0.2
Exp-surf-3	10^{-6}	10^{-6}	1000	1.5	5	0.05	0.01	0.01	0.3	0.2
Exp-surf-4	10^{-6}	10^{-6}	1000	20	20	0.2	0.04	0.04	1	0.05
Exp-surf-5	9.75×10^{-2}	1.3×10^{-5}	2581	69.7	19.4	0.155	0.139	0.039	3.6	0.052
Exp-surf-6	9.75×10^{-1}	1.3×10^{-5}	4590	39.2	21.8	0.087	0.078	0.044	1.8	0.046

Table 1: Summary of experimental parameters: names of experiments, buoyancy flux F_0, Coriolis parameter f, rotational length scale L_{rot}^{p}, dimensionless (hereafter) domain width $\widehat{L}$ and height $\widehat{H}$, source radius $\widehat{r}_s$, horizontal and vertical grid sizes $\widehat{\Delta}_h$ and $\widehat{\Delta}_z$, domain aspect ratio Γ, and natural Rossby number Ro^{*p}. *Exp-refined*, *Exp-free*, and *Exp-res* experiments are for free plumes discussed in § 3. Other experiments are for plumes constrained by boundaries discussed in § 4. Parameters in *Exp-surf-5* and *Exp-surf-6* are same as experiments shown in figures 2 and 3 in Goodman & Lenferink (2012).

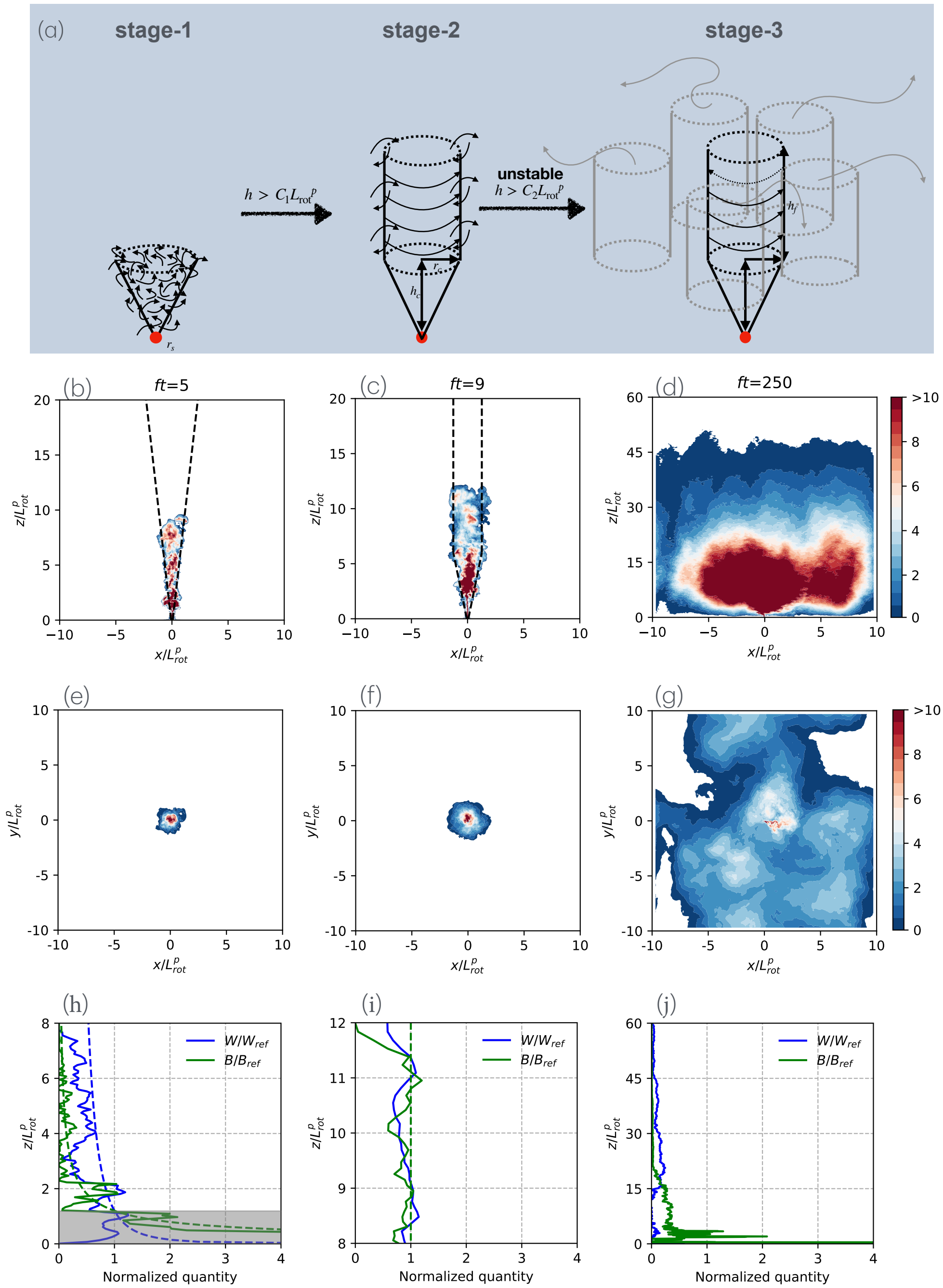

Figure 1: The three development stages of a free rotating point plume in an unstratified environment. (*a*) Diagram of three stages during plume's growth. (*b*)–(*g*) Instantaneous snapshots of the dimensionless buoyancy in the experiment *Exp-refined* in table 1: (*b*)–(*d*) side view; (*e*)–(*g*) bird's-eye view. Superscripts 'y' and 'z' denote average along $y-$ and $z-$directions, respectively. (*h*)–(*j*) Vertical profiles of normalized vertical velocity (blue) and buoyancy (green) at the plume center. The reference $W_{\rm ref}$ and $B_{\rm ref}$ in panel (*h*) are calculated from equations (3.2) and (3.3) at $z = 24r_s = 1.2L^p_{\rm rot}$, while in panels (*i*) and (*j*), they correspond to w_c and b_c (equations 3.8 and 3.9). In each panel, the theoretical predictions of geometry or vertical profiles (if exist) are represented by dashed curves.

3.2. *Stage-2: rotation-dominated cylindrical plume*

Since the plume evolves beyond one rotation period, rotation becomes important, and entrained flow from distance is deviated to form a rim current around the plume. This process inhibits lateral material/buoyancy exchange between the plume and the ambient fluid by entrainment, so that the radius of the plume remains almost constant, as can be seen in stage-2 in figure 1(*a*). The rim current speed is such that it is in thermal-wind balance with the buoyancy contrast inside and outside the plume.

In this stage, the external parameters that determine the plume are F_0 and f, which can be combined into L^p_{rot} (equation 2.1). When the plume is $O(L^p_{\mathrm{rot}})$ away from the source, the Rossby number $Ro \equiv \frac{W}{fR}$ drops below unity, demarcating the transition from the non-rotating to the rotating regime (Ma *et al.* 2020). Following Fernando *et al.* (1998) and Goodman *et al.* (2004), the transitional height h_{c} and the radius of the cylinder r_{c} follow

$$h_{\mathrm{c}} \approx 6.0 L^p_{\mathrm{rot}}, \tag{3.6}$$

$$r_{\mathrm{c}} \approx 0.7 L^p_{\mathrm{rot}}. \tag{3.7}$$

Within the plume, the vertical velocity and buoyancy are nearly homogeneous and remains constant as the plume rises. They can be estimated from the MTT solution at $z = h_{\mathrm{c}}$,

$$w_{\mathrm{c}} \approx \frac{\mu(h_{\mathrm{c}})}{\pi r_{\mathrm{c}}^2} \approx 2.2 L^p_{\mathrm{rot}} f, \tag{3.8}$$

$$b_{\mathrm{c}} \approx \frac{F_0}{\mu(h_{\mathrm{c}})} \approx 0.3 L^p_{\mathrm{rot}} f^2. \tag{3.9}$$

These scaling laws are found to align with previous lab experiments (Fernando *et al.* 1998; Goodman *et al.* 2004) and numerical experiments (Goodman & Lenferink 2012).

Figure 1(*c*) shows a snapshot at $t = 9f^{-1}$ in the reference experiment. Below the level of $z = 6L^p_{\mathrm{rot}}$, the plume retains a conical shape. However, above this level, the plume is strongly influenced by rotation, taking on a cylindrical shape with a radius of approximately L^p_{rot}. This shape aligns well with the predictions of equations (3.6) and (3.7), as indicated by the black dashed lines. In the cylindrical region, vertical velocity and buoyancy become well mixed both horizontally and vertically, broadly matching the theoretical values given by equations (3.8) and (3.9), as shown in figure 1(*i*).

However, this stage is short-lived for two reasons. First, the plume near the source is quickly deflected from the vertical and begins to precess and oscillate due to the adverse pressure gradient encountered in the rotating environment (Frank *et al.* 2017; Ma *et al.* 2020). This leads to meandering and expansion of the cylindrical plume above. Second, BCI develops, with baroclinic eddies mixing the plume with the surrounding fluid, further driving lateral expansion, as discussed in the following section.

3.3. *Stage-3: destabilized plume*

The rotation-governed cylindrical plume becomes unstable due to barotropic or baroclinic instabilities (of the rim currents), in line with Kang *et al.* (2022*a*) and Bire *et al.* (2023). After then, the plume will expand horizontally, as eddies scatter the plume fluid into the surrounding environment (stage-3 in figure 1*a*). In our experiments, the destabilization of the cylindrical plume is observed, as the plume spreads horizontally throughout the domain, with its horizontal extent far exceeding r_{c} (figures 1*d* and 1*g*) and its vertical velocity and buoyancy substantially decreasing (figure 1*j*).

In the experiments listed in the upper part of table 1, the destabilized plumes eventually stop growing in height, despite the absence of stratification. Figure 2(*a*) shows the evolution

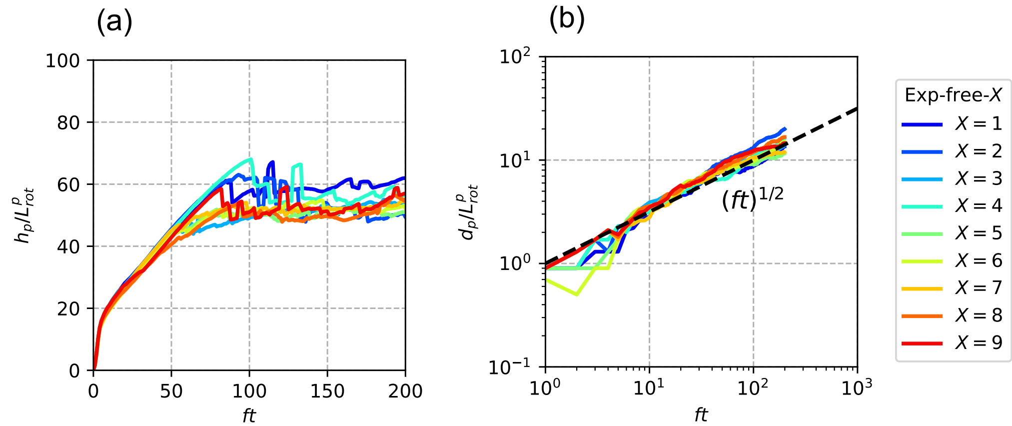

Figure 2: Evolution of (*a*) the plume height h_p and (*b*) the width d_p in the series of experiments labeled *Exp-free* in table 1. The time t is scaled by f^{-1}, and h_p and d_p are scaled by L^p_rot. In panel (*b*), the black dashed line represents the scaling $(ft)^{1/2}$.

of plume height for cases in *Exp-free*, and it is clear that all plumes plateaus at a final height h_f,

$$h_\mathrm{f} \approx (55 \pm 5) L^p_\mathrm{rot}, \tag{3.10}$$

which scales with L^p_rot. This plateau occurs around $t = 100 f^{-1}$, and from then on, the plumes only expand laterally, following $d_\mathrm{p} \sim L^p_\mathrm{rot}(ft)^{1/2}$, where d_p denotes the plume width (figure 2*b*). This phenomenon has also been observed in a fast-rotating ($Ro^{*p} = 1/60$) tank experiment conducted by Goodman *et al.* (2004) and in numerical simulations for very deep subsurface oceans in icy worlds performed by Kang *et al.* (2022*a*) and Bire *et al.* (2023). The breakdown of concentrated plumes is particularly important for icy worlds, as it dictates whether heat and materials from the vent can be transported to the ice shell without significant dilution.

Here, we propose a physical explanation for the final penetration height h_f. Inspired by Brickman (1995), Legg *et al.* (1996), and Visbeck *et al.* (1996), we hypothesize that the plume will stop growing when the lateral buoyancy scattering by eddies balances out the buoyancy injection from the source:

$$\int_0^{h_\mathrm{f}} \overline{u'b'} \cdot 2\pi r \mathrm{d}z = F_0, \tag{3.11}$$

where r is the radius of the expanded plume, and $\overline{u'b'}$ is the lateral eddy buoyancy flux, with u' being the radial eddy velocity and b' the buoyancy contrast between the plume and environment. To estimate the eddy buoyancy flux, we need scales for u' and b'. We assume that u' scales with the rim current speed U_rim as

$$u' = \gamma U_\mathrm{rim}, \tag{3.12}$$

where γ is a constant coefficient, in accordance with the theories of Eady (1949), Stone (1972), and Legg *et al.* (1996). The rim current speed U_rim can be related to b' through the thermal wind balance,

$$\frac{\partial U_\mathrm{rim}}{\partial z} = \frac{1}{f}\frac{\partial b}{\partial r} \quad \Rightarrow \quad U_\mathrm{rim} = \frac{z b'}{f r}. \tag{3.13}$$

For b', we assume that it is well-mixed within the plume, and is diluted from b_c due to the plume expansion (e.g., figures 1*d*, 1*g*, and 1*j*). Thus, it can be scaled as

$$b' = C L_{rot}^{p} f^2, \tag{3.14}$$

where $C = 0.3 r_c^2/r^2$. Here, we have used equation (3.9). Substituting all equations into the buoyancy budget equation (3.11), we obtain

$$h_f = \frac{1}{\sqrt{\pi \gamma C}} L_{rot}^{p}. \tag{3.15}$$

From numerical experiments, Legg *et al.* (1996) estimated $\gamma \approx 0.25$ for plumes in an unstratified environment. Also, in our experiments, the plume width is approximately $10L_{rot}^{p}$ when it begins to stop ascending (figure 2*b*), giving $C \approx 0.02$. Substituting these values into equation (3.15) yields

$$h_f \approx 60 L_{rot}^{p}, \tag{3.16}$$

which quantitatively agrees with our experimental measurements.

3.4. *Sensitivity test*

In our experiments, due to computational limitations, turbulent energy dissipates at the grid scale, which is significantly larger than the Kolmogorov scale. This may influence the growth of turbulent plumes. To assess whether and to what extent the model resolution affects our conclusions, we perform a mesh sensitivity study in this section. We vary $\widehat{\Delta}_h$ and $\widehat{\Delta}_z$ in a series of experiments labeled *Exp-res* in table 1. This variation effectively modifies the diffusivity and viscosity while maintaining a fixed resolution.

Lower resolution delays the onset of KHI and overestimates the height at which the plume transitions to a turbulent state, as illustrates in figure 3. Initially, the plume remains laminar due to the low Reynolds number Re, and then transits to the turbulent state as Re increases. This transition, induced by KHI, has been observed in previous laboratory experiments (e.g., Kitamura & Sumita 2011), GCM simulations (e.g., Goodman & Lenferink 2012), and direct numerical simulations (e.g., Ward 2022). The critical height and time for this transition are found to scale with

$$L_\kappa \equiv \left(\frac{\kappa^3}{F_0}\right)^{\frac{1}{2}}, \quad t_\kappa \equiv \frac{\kappa^2}{F_0}, \tag{3.17}$$

where κ is the diffusivity (Ward 2022). In low-resolution experiments, turbulent energy dissipates at larger scales, leading to larger effective κ. This delays the onset of KHI and allows the laminar plume to penetrate to higher heights, potentially exceeding h_c (top left panel in figure 3). Consequently, the MTT stage does not emerge and the plume transits directly into a rotationally dominant cylinder (top-right panel in figure 3). As resolution increases, smaller-scale turbulence is better resolved, leading to an earlier onset of KHI and the transition to the turbulent plume. This allows the MTT stage to develop and be accurately captured (lower row in figure 3).

Furthermore, lower resolution overestimates the final penetration height h_f, as shown in the central panel of figure 3. This is because the laminar plume in the earlier stage penetrates too high (top-left panel in figure 3). Additionally, a lower-resolution mesh has a reduced ability to resolve small-scale baroclinic eddies, leading to an underestimate of lateral eddy buoyancy flux, which also contributes to a higher penetration height. As the resolution increases, h_f converges to approximately $55L_{rot}^{p}$, demonstrating that the mesh adopted before with $\widehat{\Delta}_h = \widehat{\Delta}_z = 0.1$ is sufficient to capture the destabilized plume induced by BCI, while

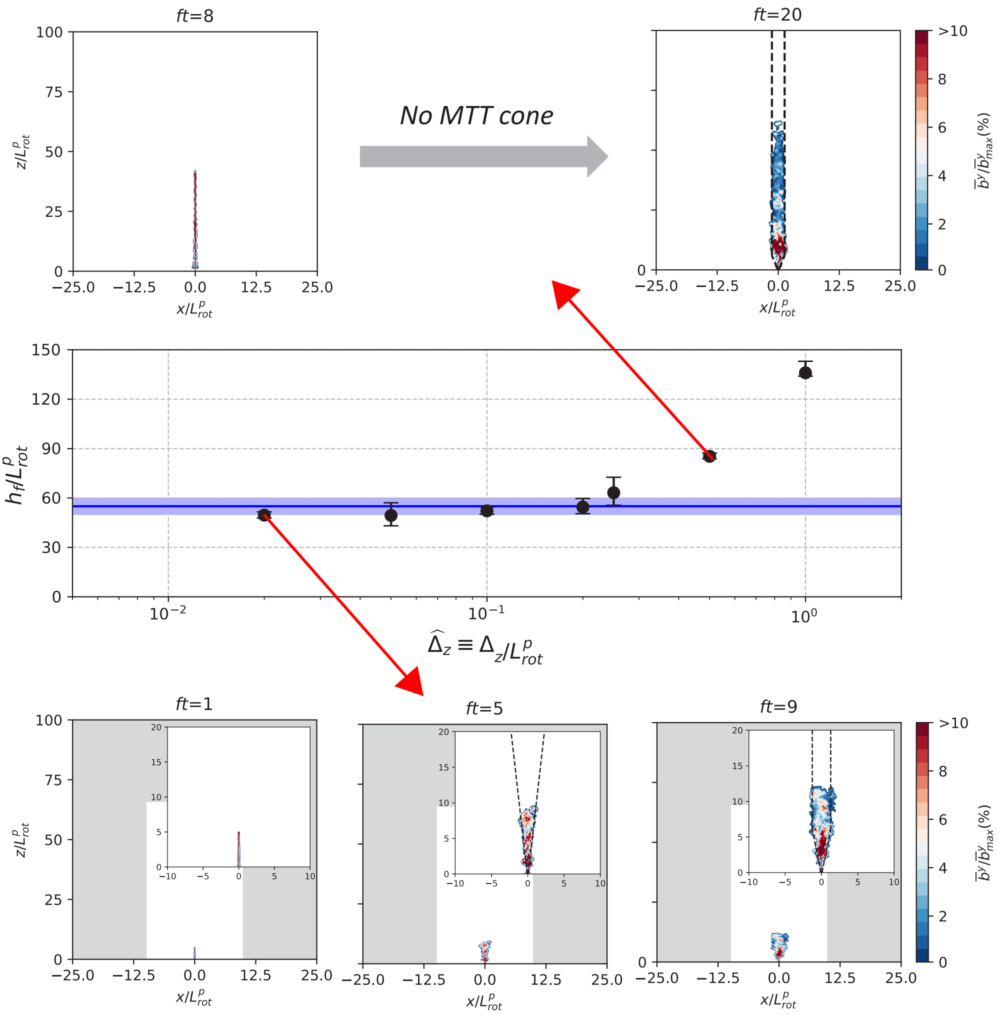

Figure 3: Center: Final penetration height h_f on meshes with different dimensionless (vertical) resolutions. Data points represent the average over the time interval from $ft = 100$ to $ft = 200$, with error bars indicating the maximum and minimum values within this interval. Blue line and shading represent $(55 \pm 5)L^p_{\mathrm{rot}}$. Upper and lower rows: Side views of the plume shape during its evolution in experiments *Exp-res-4* and *Exp-refined*, respectively. In lower-row panels, gray shading covers the region out of the domain. Several zoomed-in panels are included. Theoretical geometry predictions (if exist) are represented by dashed curves.

minimizing the influence of variations in the onset time of KHI. Consequently, the measured h_{f} (equation 3.10) is robust.

We also adopt different domain extents $\widehat{L}$ and $\widehat{H}$ in *Exp-refined*, *Exp-free-8*, *Exp-free-9*, and *Exp-res-1*. The similar plume evolution and h_{f} shown in figure 2 demonstrate that these domain sizes are sufficient to ensure that the plume is not influenced by boundaries.

4. Development of a constrained point plume by boundaries

In this section, we investigate the development of point plumes constrained by domain boundaries, with a particular focus on plume patterns upon encountering the upper boundary. The upper boundary represents either a free surface or an ice shell that covers lakes or oceans.

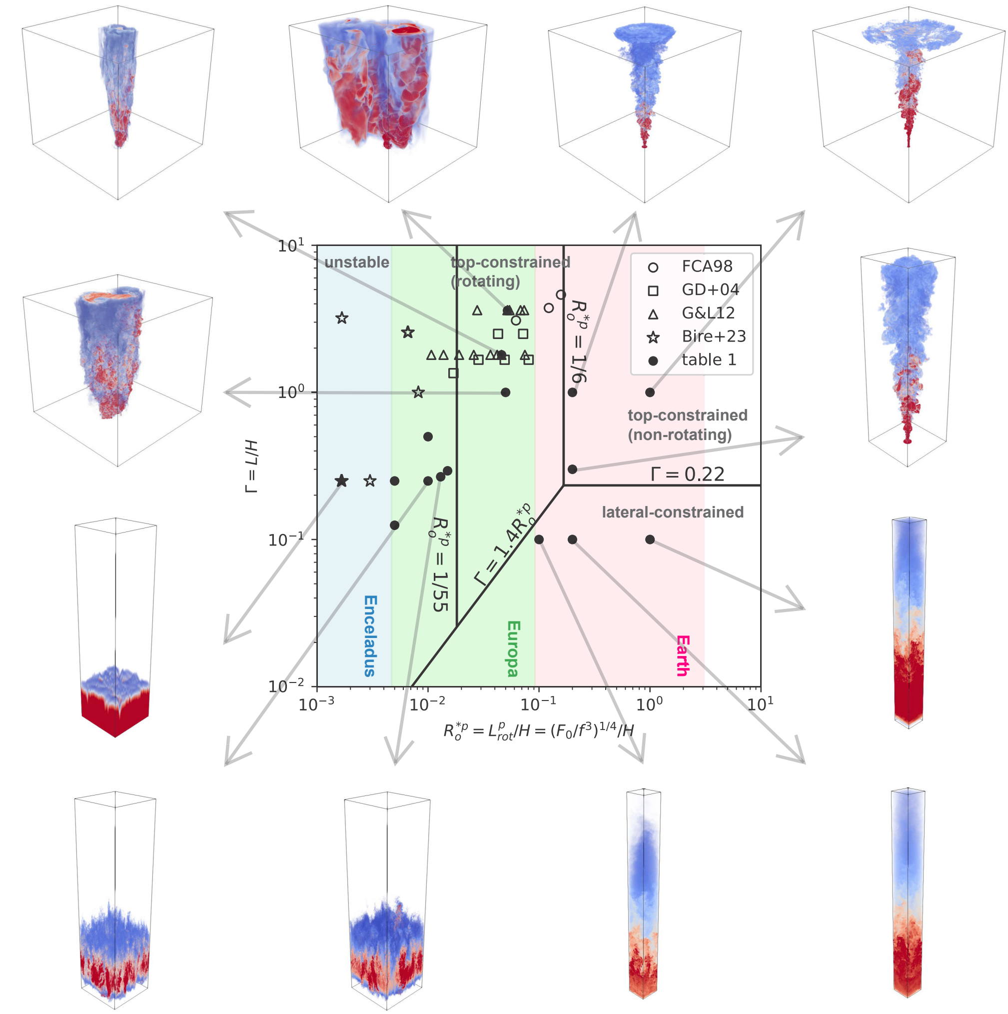

Figure 4: Parameter diagram for constrained plumes by boundaries (center panel) and simulated plume structures represented by isosurfaces of buoyancy (surrounding panels). The $x-$ and $y-$axes are natural Rossby number for point plumes Ro^{*p} and domain aspect ratio Γ, respectively. Circles, squares, triangles, stars, and black dots mark the water tank experiments in Fernando *et al.* (1998) (FCA98) and Goodman *et al.* (2004) (GD+04), and numerical experiments in Goodman & Lenferink (2012) (G&L12), Bire *et al.* (2023) (Bire+23), and this paper (table 1), respectively. Boundaries for four regimes are obtained from equations (3.1), (3.6), (3.7), and (3.10). The parameter regimes for Earth (global-mean $f = 4.4 \times 10^{-5}$ s^{-1}, gravity $g = 9.8$ m s^{-2}, thermal expansivity $\alpha = 3 \times 10^{-4}$ K^{-1}, heat flux $Q \leqslant 10$ GW, and ocean depth $H = 3$ km), Europa (global-mean $f = 1.3 \times 10^{-5}$ s^{-1}, $g = 1.3$ m s^{-2}, $\alpha = 3 \times 10^{-4}$ K^{-1}, heat flux $Q \leqslant 10$ GW, and ocean depth $H = 50 \sim 100$ km), and the south pole of Enceladus ($f = 1 \times 10^{-4}$ s^{-1}, $g = 0.1$ m s^{-2}, $\alpha = 10^{-5}$ K^{-1}, heat flux $Q \leqslant 5$ GW, and ocean depth $H = 40$ km) are represented by pink, light green, and light blue shading, respectively.

With the horizontally periodic domain, we represent a point-plume array that may interact with each other during their development. The domain width thus corresponds to the distance between two point sources.

Here, the parameters that determine the dynamics of the plume are $(L,\ H,\ L^p_{\text{rot}})$, which

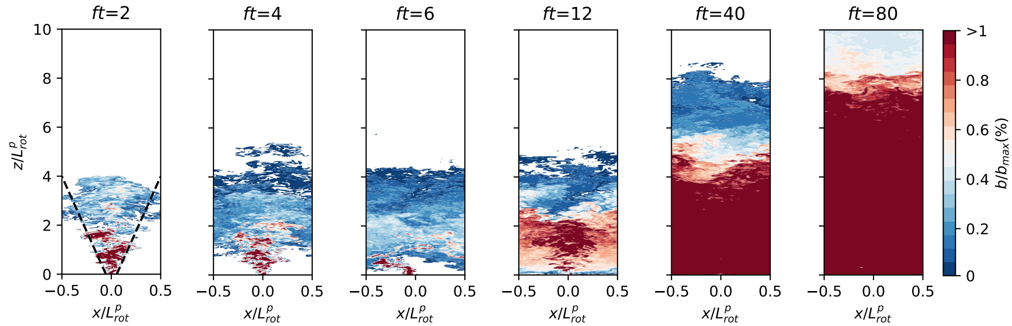

Figure 5: Instantaneous $x-z$ cross-sections of dimensionless buoyancy $b/b_{\max}$ along $y = 0$ in the experiment *Exp-wall-3* in table 1. Dashed lines represent the plume geometry predicted by MTT model (equation 3.1).

are combined into Γ and Ro^{*p} (equation 2.3). In the parameter space spanned by these two non-dimensional numbers, we identify the following four regimes (figure 4):

(1) **Lateral-constrained regime**: The domain is too narrow to fit either the non-rotating conical plume, i.e. $\Gamma < 0.22$ (equation 3.1), or the rotation-dominated cylindrical plume, i.e. $\Gamma < 1.4Ro^{*p}$ (equation 3.7). In this regime, the plume will encounter the lateral boundary and become well mixed, so that it cannot remain concentrated when reaching the top boundary.

(2) **Top-constrained regime (non-rotating)**: The domain is shallow, so the plume will encounter the top boundary as a cone without being influenced by rotation, i.e. $Ro^{*p} > 1/6$ (equation 3.6). However, it is wide enough to fit this conical plume, i.e. $\Gamma > 0.22$ (equation 3.1). In this regime, the plume remains concentrated upon impacting the upper boundary.

(3) **Top-constrained regime (rotating)**: The rotation is sufficiently fast to constrain the plume into a cylinder before it reaches the top boundary, i.e. $Ro^{*p} < 1/6$ (equation 3.6). In addition, the domain is wide enough to fit this cylindrical plume, i.e. $\Gamma > 1.4Ro^{*p}$ (equation 3.7). In this regime, the plume remains cylindrical and concentrated upon impacting the upper boundary.

(4) **Unstable regime**: Strongly rotating plumes whose final penetration depth h_{f} is smaller than domain depth, i.e. $Ro^{*p} < 1/55$ (equation 3.10), in a wide enough domain to fit the cylindrical plume, i.e. $\Gamma > 1.4Ro^{*p}$ (equation 3.7), will become unstable before encountering the upper surface. In this regime, the pattern of the buoyancy source is not maintained.

4.1. *Lateral-constrained regime*

To investigate the plume pattern that will first encounter lateral boundaries (equivalent to interactions with other plumes), we carried out three experiments that satisfy the criterion for the lateral-constrained regime, labeled *Exp-wall* in table 1. The plumes in these experiments exhibit similar behavior (bottom-right panels in figure 4).

Snapshots of $b/b_{\max}$ at different time steps in *Exp-wall-3* are illustrated in figure 5. The plume is found to encounter the lateral boundaries at $z \approx 4L^p_{\mathrm{rot}}$, consistent with the prediction of MTT. Thereafter, the plume merges with adjacent plumes and becomes horizontally well-mixed. This indicates that fluid above this level only “sees” a uniformly distributed buoyancy flux, regardless of the buoyancy flux pattern at the bottom. Over time, these plumes first fill the lower part of the domain with high-buoyancy fluid, because the plume’s upwelling must be balanced by surrounding downwelling. Only after the lower domain becomes well mixed

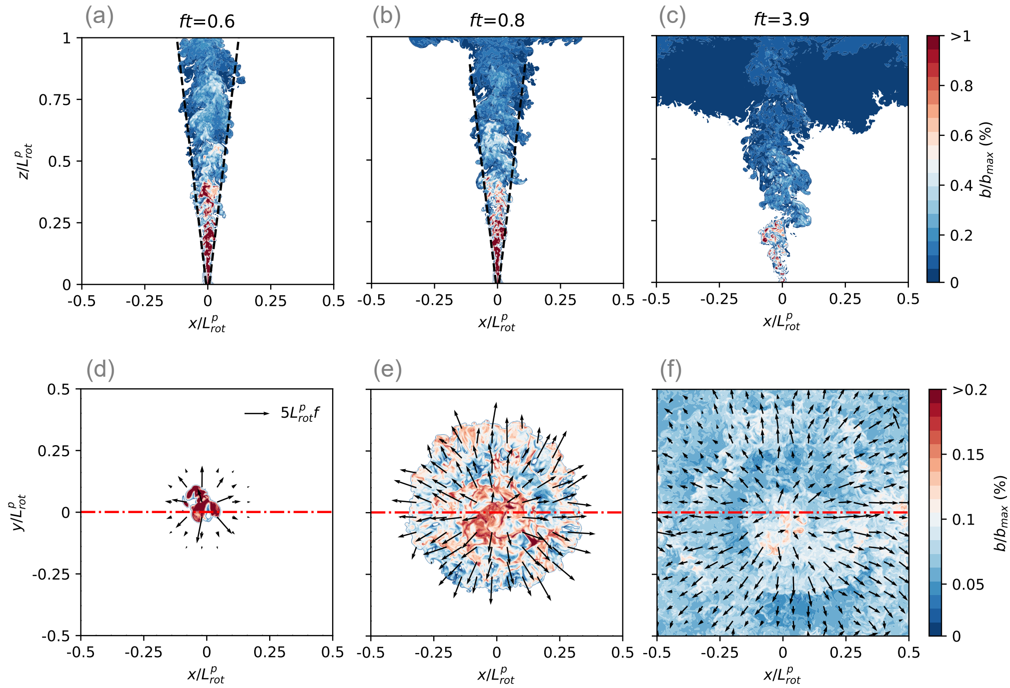

Figure 6: Instantaneous views of dimensionless buoyancy $b/b_{\max}$ (color shading) and horizontal flows (vectors) in the experiment *Exp-surf-1* in table 1: (*a*)–(*c*) $x-z$ cross-sections along red dotted lines in the lower row; (*d*)–(*f*) $x-y$ cross-sections at the top. Theoretical geometry predictions (if exist) are represented by black dashed lines.

does the high-buoyancy fluid begin to fill the upper domain, consistent with the "filling-box" effect described by Baines & Turner (1969) and Turner (1969).

4.2. *Top-constrained regimes*

To investigate the plume pattern that will first encounter the top boundary, we conduct a series of experiments labeled *Exp-surf* in table 1, which include both weakly rotating cases (*Exp-surf-1* to *Exp-surf-3*) and strongly rotating cases (*Exp-surf-4* to *Exp-surf-6*).

If $Ro^{*p} > 1/6$, rotation has no effect on the rising plume, so the plume maintains the cone shape predicted by the MTT model (equation 3.1) until it meets the upper boundary, as shown in figures 6(*a*) and 6(*d*). After that, the buoyant fluid spreads horizontally along the top boundary, forming an anvil layer (figures 6*b* and 6*e*). This behavior is similarly reported in tank experiments by Fernando *et al.* (1998). Eventually, if the domain is relatively narrow, the plume will fill the plane and be pushed downward under the influence of the "filling-box" effect discussed in § 4.1 (figures 6*c* and 6*f*). Otherwise, the effect of rotation will eventually dominate, forming anticyclonic flows around a confined plume (figure not shown here).

If $Ro^{*p} < 1/6$, rotation would have already started to modulate the plume before encountering the top boundary. As demonstrated in Goodman *et al.* (2004), in this case, the plume undergoes the first two stages sketched in figure 1(*a*), and impacts the upper boundary as a cylindrical plume, generating anticyclonic flows (figures 7*a*, 7*b*, and 7*e*). Then, the cylindrical plume expands outward due to mass conservation, evolving from the cylinder into a baroclinic cone (figure 7*a*, 7*c*, and 7*f*). The radius of the cone scales with

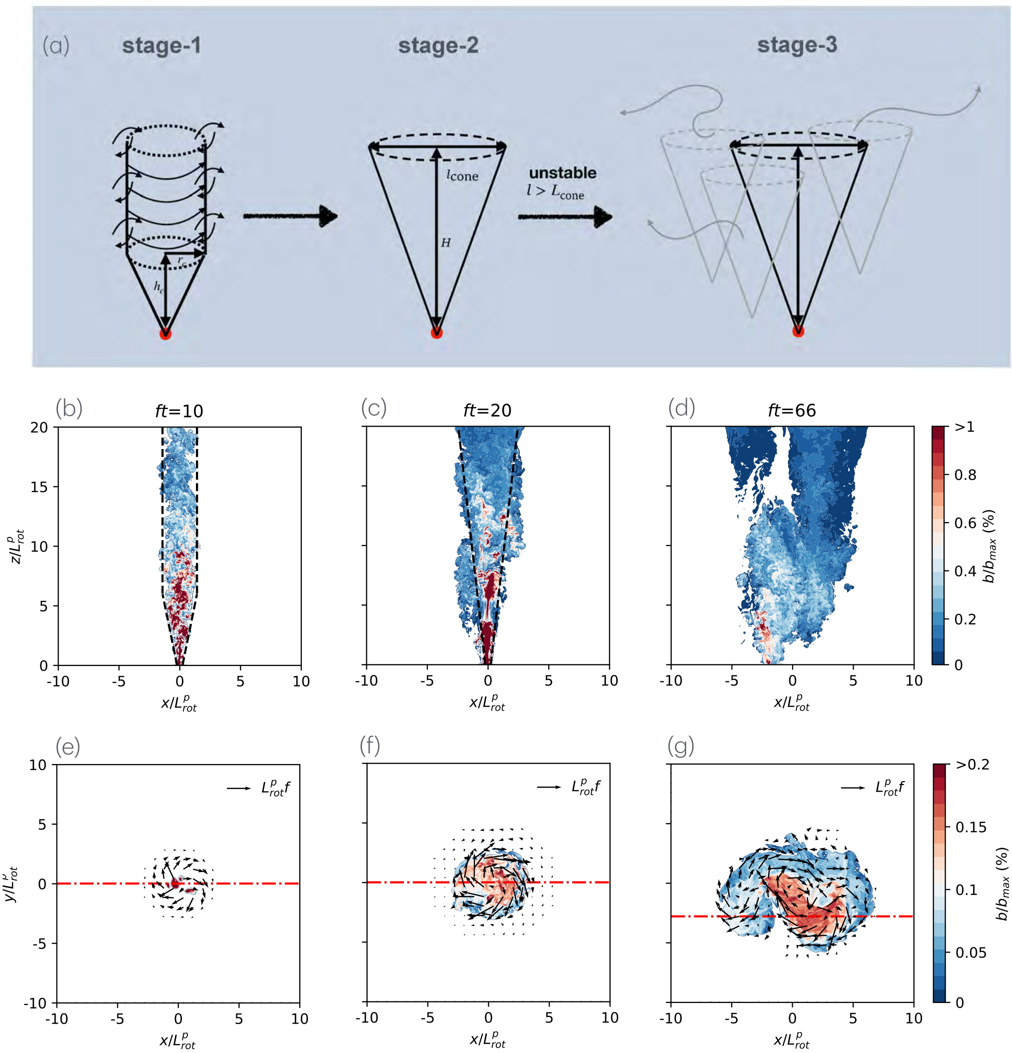

Figure 7: Development of a rotating plume after encountering the top boundary. (*a*) Diagram of three stages during plume's growth. (*b*)–(*g*) Same as figure 6 but for the experiment *Exp-surf-4* in table 1.

$L_{\text{cone}} = \sqrt{b'H}/f \sim L^p_{\text{rot}}/\sqrt{Ro^{*p}}$ (Fernando *et al.* 1998; Goodman *et al.* 2004; Goodman & Lenferink 2012), which is the Rossby deformation radius for a two-layer fluid (Pedlosky 1987). We validated this cone scaling though the results are not shown here. Finally, due to baroclinic instability, the primary cone breaks down into multiple secondary conical vortices (two vortices in figures 7*d* and 7*g*). The numbers of these vortices can be estimated using a “heton” model, as shown by Legg & Marshall (1993) and Legg *et al.* (1996).

5. Effect of finite source size

When the source size exceeds the size of the plume characterized by the rotational length scale L^p_{rot}, i.e. $\hat{r}_s \gtrsim 1$, the source can no longer be treated as a geometric point, but rather a circular region with finite area. This scenario is analogous to convection driven by a wide-range buoyancy source in laboratory experiments (Maxworthy & Narimousa 1994; Brickman

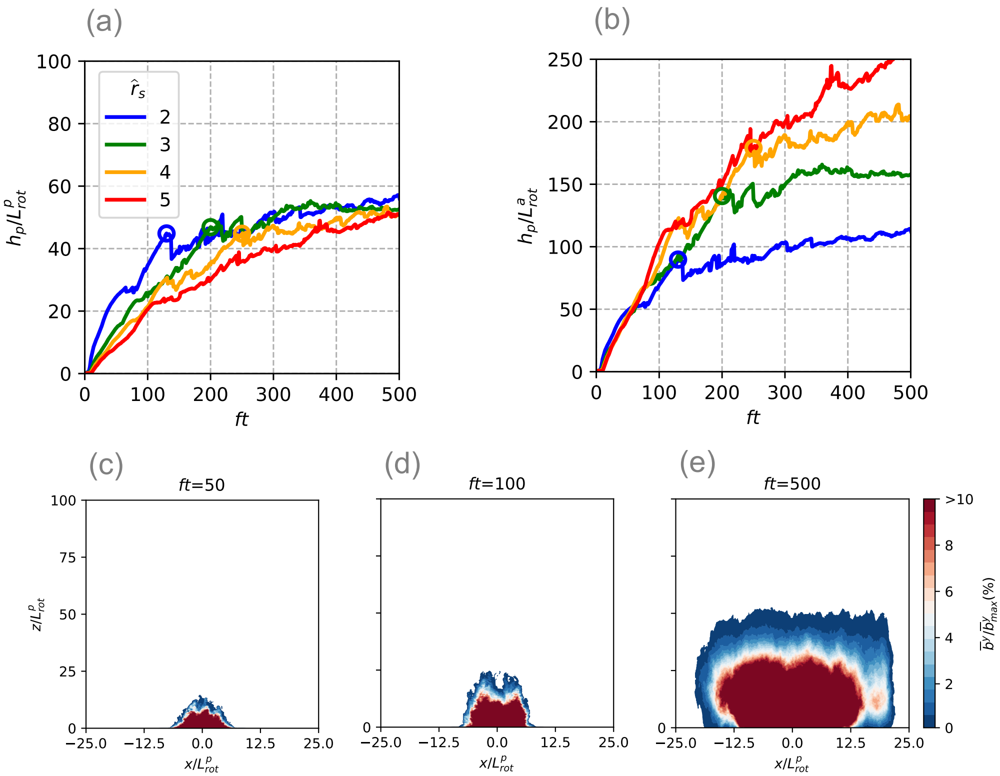

Figure 8: Evolution of the plume height h_p (*a*) scaled by L^p_rot and (*b*) by L^a_rot in experiments with wide-range source. Colored circles mark the onset time at which the increase in h_p significantly slows. (*c*)–(*e*) Side views of plume shape during its evolution in the experiment with $\widehat{r}_\mathrm{s} = 3$ (green curve in panels *a* and *b*).

1995; Narimousa 1997) and open ocean convection on Earth (Jones & Marshall 1993; Send & Marshall 1995; Legg *et al.* 1996; Visbeck *et al.* 1996).

With the domain size fixed at $\widehat{L} = 50$ and $\widehat{H} = 100$ and the resolution set to $\widehat{\Delta}_h = \widehat{\Delta}_z = 0.1$, we conduct experiments with different source radii, $\widehat{r}_\mathrm{s} = 2, 3, 4$ and 5. Since the source radius r_s is larger than the columnar plume radius r_c, the buoyant fluid emanating from the source has an almost Gaussian-like envelope (figure 8*c*), following the buoyancy flux prescribed at the bottom. Subsequently, the plume forms a cylindrical shape with a radius close to $\widehat{r}_\mathrm{s}$ (figure 8*d*). This cylinder then expands laterally, in a way that is similar to point plumes (figure 8*e*), which eventually cause plume height to plateau at $h_\mathrm{f} \sim 60L^p_\mathrm{rot}$ (figure 8*a*), similar to that for point plumes.

It is also evident from figure 8(*a*) that although the final states of the plumes forced by heat sources of different sizes are similar to each other, the plume height evolutions during their early stages diverge (to the left of the circles in figure 8*a*). As the heat source widens, the plume rises at a slower rate initially. This is because a larger $\widehat{r}_\mathrm{s}$ results in a smaller buoyancy flux per unit area, which now primarily governs plume dynamics rather than the total buoyancy flux. Consequently, when nondimensionalized by L^a_rot (equation 2.4), the early evolution of the plume height from experiments with different $\widehat{r}_\mathrm{s}$ collapses into one line (to the left of the circles in figure 8*b*). Although the initial development of the plume diverges from the L^p_rot scaling, it does not carry over to the final stage, which sets the penetration height h_f. This is because, in all of our experiments, the cylindrical plume is already wide enough to cover the entire buoyancy source before reaching h_f (figure 8*d*). Then, the argument that determines the penetration height of the point plume would also apply here, leading to a similar h_f.

6. Summary and discussion

In this study, we investigate rotating plumes in an unstratified environment that are generated by localized buoyant sources at the bottom. We start by considering a plume freely developing without interfering with lateral or top boundaries, then proceed to account for boundary effects, which allows us to determine under which conditions the pattern of buoyancy source can project onto the upper surface.

A rotating point plume that grows freely generally undergoes three stages. In stage-1, with negligible rotation effect, the plume rises as a cone, accompanied by diluted upward velocity and buoyancy (figures 1*a*, 1*b*, 1*e*, and 1*h*). During this stage, its geometry and dynamics are well described by the MTT model (equations 3.1–3.3; Morton *et al.* 1956). In stage-2, rotation becomes important and forces the plume into a cylindrical shape, within which both momentum and buoyancy are almost uniform (figures 1*a*, 1*c*, 1*f*, and 1*i*). The geometry and dynamics of this cylindrical plume follow the scaling laws (3.6)–(3.9) (also see Fernando *et al.* 1998; Goodman *et al.* 2004). In stage-3, the plume becomes barotropically or baroclinically unstable, leading to lateral loss of mass and buoyancy through eddy transport, which hinders its upward penetration (figure 1*a*, 1*d*, 1*g*, and 1*j*).

We find that freely developed plumes cease to rise at a height h_f, as the total buoyancy flux released by the source is completely leaked to the ambient by lateral eddy flux (figure 2). Based on this point, we propose a scaling law

$$h_f \approx 55 L_{rot}^{p}. \tag{6.1}$$

Here, $L_{rot}^{p} = (F_0 f^{-3})^{\frac{1}{4}}$ represents the characteristic scale of a rotating plume that is larger than the source size, meaning the source can be treated as a point. When the source size exceeds the plume scale, the source should be treated as a circular area. The early evolution of the plume is then mainly determined by the buoyancy flux per unit area, which leads to the relevant rotational length scale $L_{rot}^{a} = (F_0 f^{-3} r_s^{-2})^{\frac{1}{2}}$. However, the final penetration height h_f is close to that of point plumes, since its lateral extend is as wide as the source, which means that the majority of F_0 is contained within the plume (figure 8).

Taking into account the constraints imposed by the boundaries, the evolution of plumes largely depends on their geometry upon encountering these boundaries. We identify four regimes in the non-dimensional parameter space defined by the domain aspect ratio $\Gamma = L/H$ and the natural Rossby number for point plumes $Ro^{*p} = L_{rot}^{p}/H$, summarized in figure 4. Only in two top-constrained regimes is the pattern of the bottom buoyancy flux preserved when the upper surface is impacted.

In deep convective regions of the Earth in winter, the heat lost to the atmosphere can reach up to 800 W m^{-2} and persist for tens of days, corresponding to buoyancy flux per unit area ranging from 10^{-8} to 10^{-7} m^2 s^{-3} (Jones & Marshall 1993; Marshall & Schott 1999). The plumes generated in these regions have horizontal scales ranging from several hundred meters to one kilometer, corresponding to h_f greater than 6 km (equation 3.10), double the mean depth of the ocean. As a result, the dense cold water can easily descend to the sea floor, forming deep water masses (Jones & Marshall 1993; Send & Marshall 1995). Furthermore, localized hydrothermal vents exhibit heat fluxes ranging from 1 MW to 10 GW (Thomson *et al.* 1992), corresponding to total buoyancy fluxes ranging from 10^{-3} to 10 m^4 s^{-3}. Plumes generated by such vents typically have scales greater than 100 m and can transport to the surface if the ocean is unstratified (equation 3.10), as shown in figure 4 where we estimate parameter space for Earth's oceans (pink regions).

Icy satellites, such as Europa (the second moon of Jupiter) and Enceladus (the second moon of Saturn), have been found to host deep global subsurface oceans and exhibit ongoing geological activities (Anderson *et al.* 1998; Hansen *et al.* 2006; Porco *et al.* 2006; Collins & Goodman 2007). On Europa, the ocean may be 50–100 km deep (Goodman & Lenferink 2012), and the heat flux for hydrothermal systems is on the order of 0.1–10 GW (Lowell & DuBose 2005; Goodman & Lenferink 2012). On Enceladus, the ocean may be 40 km deep (Thomas *et al.* 2016), and the hydrothermal heat flux may range from <0.1 GW following Vance & Goodman (2009) to 5 GW following Choblet *et al.* (2017). In figure 4, we mark the parameter space for potential hydrothermal plumes on these two moons in light green (Europa) and light blue (Enceladus). The strongest possible plumes on Europa fall into the (rotating) top-constrained regime, suggesting that plumes are able to encounter the ice shell. This aligns with the conclusions from the numerical experiments conducted for Europa by Goodman & Lenferink (2012), two of which are repeated (*Exp-surf-5* and *Exp-surf-6*) and are shown in the top left of figure 4. As for Enceladus, all scenarios considered fall into an unstable regime, suggesting that detecting the pattern of hydrothermal vents from the surface may be challenging and that nutrients and biosignatures emanated from the hydrothermal vents are likely well-mixed when delivered to the water-ice interface, in line with Kang *et al.* (2022*a*) and Bire *et al.* (2023).

Acknowledge. This project uses Oceananigans, an open-source ocean general circulation model. The authors thank Ali Ramadhan, Simone Silvestri, Gregory L. Wagner, and Xin Kai Lee for technical support for Oceananigans, the MIT Satori Group for support with computing resources, and Kaushal Gianchandni, Peter Higgins, and Yuchen Ma for helpful discussion.

Funding. WK acknowledges support from startup funding. JM acknowledges support from NASA Astrobiology Grant 80NSSC19K1427 "Exploring Ocean World".

Declaration of interests. The authors report no conflict of interest.

Data availability statement. All the data supporting this work are available from the corresponding author upon reasonable request.

Author ORCIDs. Shuang Wang, https://orcid.org/0000-0002-9406-1781; Wanying Kang, https://orcid.org/0000-0002-4615-3702; Yixiao Zhang, https://orcid.org/0000-0001-6194-760X; John Marshall, https://orcid.org/0000-0001-9230-3591

REFERENCES

Abdalla, Ibrahim E., Cook, Malcolm J. & Hunt, Gary R. 2009 Numerical study of thermal plume characteristics and entrainment in an enclosure with a point heat source. *Engineering Applications of Computational Fluid Mechanics* **3** (4), 608–630.

Anderson, J. D., Schubert, G., Jacobson, R. A., Lau, E. L., Moore, W. B. & Sjogren, W. L. 1998 Europa's differentiated internal structure: Inferences from four galileo encounters. *Science* **281** (5385), 2019–2022.

Ashkenazy, Yosef, Gildor, Hezi, Losch, Martin, Macdonald, Francis A, Schrag, Daniel P. & Tziperman, Eli 2013 Dynamics of a snowball earth ocean. *Nature* **495** (7439), 90 – 93.

Baines, P. G. & Sparks, R. S. J. 2005 Dynamics of giant volcanic ash clouds from supervolcanic eruptions. *Geophysical Research Letters* **32** (24).

Baines, W. D. & Turner, J. S. 1969 Turbulent buoyant convection from a source in a confined region. *Journal of Fluid Mechanics* **37** (1), 51–80.

Bhaganagar, Kiran & Bhimireddy, Sudheer R. 2020 Numerical investigation of starting turbulent buoyant plumes released in neutral atmosphere. *Journal of Fluid Mechanics* **900**, A32.

Bire, Suyash, Kang, Wanying, Ramadhan, Ali, Campin, Jean-Michel & Marshall, John 2022

Exploring ocean circulation on icy moons heated from below. *Journal of Geophysical Research: Planets* **127** (3), e2021JE007025.

Bire, Suyash, Mittal, Tushar, Kang, Wanying, Ramadhan, Ali, Tuckman, Philip J., German, Christopher R., Thurnherr, Andreas M. & Marshall, John 2023 Divergent behavior of hydrothermal plumes in fresh versus salty icy ocean worlds. *Journal of Geophysical Research: Planets* **128** (11), e2023JE007740.

Boubnov, B. M. & van Heijst, G. J. F. 1994 Experiments on convection from a horizontal plate with and without background rotation. *Experiments in Fluids* **16** (3), 155–164.

Brickman, David 1995 Heat flux partitioning in open-ocean convection. *Journal of Physical Oceanography* **25** (11), 2609 – 2623.

Choblet, Gaël, Tobie, Gabriel, Sotin, Christophe, Běhounková, Marie, Čadek, Ondřej, Postberg, Frank & Souček, Ondřej 2017 Powering prolonged hydrothermal activity inside enceladus. *Nature Astronomy* **1** (12), 841–847.

Collins, Geoffrey C. & Goodman, Jason C. 2007 Enceladus' south polar sea. *Icarus* **189** (1), 72–82.

Eady, E. T. 1949 Long waves and cyclone waves. *Tellus* **1** (3), 33–52.

Fernando, H. J. S., Chen, R-r. & Ayotte, B. A. 1998 Development of A Point Plume in the Presence of Background Rotation. *Physics of Fluids* **10** (9), 2369–2383.

Fernando, Harindra J. S., Chen, Rui-Rong & Boyer, Don L. 1991 Effects of rotation on convective turbulence. *Journal of Fluid Mechanics* **228**, 513–547.

Ferrero, Enrico, Salizzoni, Pietro, Ive, Federica, Manfrin, Massimiliano, Forza, Renato, Bisignano, Andrea & Mortarini, Luca 2022 Effect of rotation on buoyant plume dynamics. *Heat and Mass Transfer* **58** (7).

Frank, D., Landel, J. R., Dalziel, S. B. & Linden, P. F. 2017 Anticyclonic precession of a plume in a rotating environment. *Geophysical Research Letters* **44** (18), 9400–9407.

Goodman, Jason C., Collins, Geoffrey C., Marshall, John & Pierrehumbert, Raymond T. 2004 Hydrothermal plume dynamics on europa: Implications for chaos formation. *Journal of Geophysical Research: Planets* **109** (E3).

Goodman, Jason C. & Lenferink, Erik 2012 Numerical simulations of marine hydrothermal plumes for europa and other icy worlds. *Icarus* **221** (2), 970–983.

Hansen, Candice J, Esposito, L, Stewart, A I F, Colwell, J, Hendrix, A, Pryor, W, Shemansky, D & West, R 2006 Enceladus' Water Vapor Plume. *Science* **311** (5766), 1422–1425.

Jones, Helen & Marshall, John 1993 Convection with rotation in a neutral ocean: A study of open-ocean deep convection. *Journal of Physical Oceanography* **23** (6), 1009 – 1039.

Kang, Wanying, Marshall, John, Mittal, Tushar & Bire, Suyash 2022*a* Ocean dynamics and tracer transport over the south pole geysers of enceladus. *Monthly Notices of the Royal Astronomical Society* **517** (3), 3485–3494.

Kang, Wanying, Mittal, Tushar, Bire, Suyash, Campin, Jean-Michel & Marshall, John 2022*b* How does salinity shape ocean circulation and ice geometry on enceladus and other icy satellites? *Science Advances* **8** (29), eabm4665.

Kitamura, Shogo & Sumita, Ikuro 2011 Experiments on a turbulent plume: Shape analyses. *Journal of Geophysical Research: Solid Earth* **116** (B3).

Legg, Sonya, Jones, Helen & Visbeck, Martin 1996 A heton perspective of baroclinic eddy transfer in localized open ocean convection. *Journal of Physical Oceanography* **26** (10), 2251 – 2266.

Legg, Sonya & Marshall, John 1993 A heton model of the spreading phase of open-ocean deep convection. *Journal of Physical Oceanography* **23** (6), 1040 – 1056.

List, E. John 1982 Turbulent jets and plumes. *Annual Review of Fluid Mechanics* **14**, 189–212.

List, E. J. & Imberger, Jörg 1973 Turbulent entrainment in buoyant jets and plumes. *Journal of the Hydraulics Division* **99** (9), 1461–1474.

Lowell, Robert P. & DuBose, Myesha 2005 Hydrothermal systems on europa. *Geophysical Research Letters* **32** (5).

Lupton, J. E., Delaney, J. R., Johnson, H. P. & Tivey, M. K. 1985 Entrainment and vertical transport of deep-ocean water by buoyant hydrothermal plumes. *Nature* **316** (6029), 621 – 623.

Ma, Yongxing, Flynn, Morris R. & Sutherland, Bruce R. 2020 Plumes in a rotating two-layer stratified fluid. *Environmental Fluid Mechanics* **20** (1), 103–122.

Marshall, John & Schott, Friedrich 1999 Open-ocean convection: Observations, theory, and models. *Reviews of Geophysics* **37** (1), 1–64.

MAXWORTHY, T. 1997 Convection into domains with open boundaries. *Annual Review of Fluid Mechanics* **29** (Volume 29, 1997), 327–371.

MAXWORTHY, T. & NARIMOUSA, S. 1994 Unsteady, turbulent convection into a homogeneous, rotating fluid,with oceanographic applications. *Journal of Physical Oceanography* **24** (5), 865 – 887.

MORTON, B. R., TAYLOR, GEOFFREY INGRAM & TURNER, JOHN STEWART 1956 Turbulent gravitational convection from maintained and instantaneous sources. *Proceedings of the Royal Society of London. Series A. Mathematical and Physical Sciences* **234** (1196), 1–23.

NARIMOUSA, SIAVASH 1997 Dynamics of mesoscale vortices generated by turbulent convection at large aspect ratios. *Journal of Geophysical Research: Oceans* **102** (C3), 5615–5624.

OKADA, NAOSUKE, IKEDA, MOTOYOSHI & MINOBE, SHOSHIRO 2004 Numerical experiments of isolated convection under polynya. *Journal of Oceanography* **60** (6), 927 – 943.

PEDLOSKY, JOSEPH 1987 *Geophysical Fluid Dynamics*. Springer New York.

PORCO, CAROLYN C, HELFENSTEIN, PAUL, THOMAS, PC, INGERSOLL, AP, WISDOM, J, WEST, ROBERT, NEUKUM, GERHARD, DENK, TILMANN, WAGNER, ROLAND, ROATSCH, THOMAS & OTHERS 2006 Cassini observes the active south pole of enceladus. *science* **311** (5766), 1393–1401.

RAMADHAN, ALI, WAGNER, GREGORY LECLAIRE, HILL, CHRIS, CAMPIN, JEAN-MICHEL, CHURAVY, VALENTIN, BESARD, TIM, SOUZA, ANDRE, EDELMAN, ALAN, FERRARI, RAFFAELE & MARSHALL, JOHN 2020 Oceananigans.jl: Fast and Friendly Geophysical Fluid Dynamics on GPUs. *Journal of Open Source Software* **5** (53), 2018.

ROUSE, HUNTER, SHUN YIH, CHIA & HUMPHREYS, H. W. 1952 Gravitational convection from a boundary source. *Tellus A: Dynamic Meteorology and Oceanography* **4** (3), 201–210.

SCHOTT, FRIEDRICH & LEAMAN, KEVIN D. 1991 Observations with moored acoustic doppler current profilers in the convection regime in the golfe du lion. *Journal of Physical Oceanography* **21** (4), 558 – 574.

SEND, UWE & MARSHALL, JOHN 1995 Integral effects of deep convection. *Journal of Physical Oceanography* **25** (5), 855 – 872.

SPEER, K. G. & MARSHALL, J. 1995 The growth of convective plumes at seafloor hot springs. *Journal of Marine Research* pp. 1025–1057.

STONE, PETER H. 1968 Some properties of hadley regimes on rotating and non-rotating planets. *Journal of Atmospheric Sciences* **25** (4), 644 – 657.

STONE, PETER H. 1972 A simplified radiative-dynamical model for the static stability of rotating atmospheres. *Journal of Atmospheric Sciences* **29** (3), 405 – 418.

THOMAS, P.C., TAJEDDINE, R., TISCARENO, M.S., BURNS, J.A., JOSEPH, J., LOREDO, T.J., HELFENSTEIN, P. & PORCO, C. 2016 Enceladus's measured physical libration requires a global subsurface ocean. *Icarus* **264**, 37–47.

THOMSON, RICHARD E., DELANEY, JOHN R., MCDUFF, RUSSELL E., JANECKY, DAVID R. & MCCLAIN, JAMES S. 1992 Physical characteristics of the endeavour ridge hydrothermal plume during july 1988. *Earth and Planetary Science Letters* **111** (1), 141–154.

TURNER, J S 1969 Buoyant plumes and thermals. *Annual Review of Fluid Mechanics* **1** (Volume 1, 1969), 29–44.

TURNER, J. S. 1973 *Buoyancy Effects in Fluids*. Cambridge University Press.

VANCE, STEVEN & GOODMAN, JASON 2009 *Oceanography of an Ice-Covered Moon. In: Pappalardo, R.T., McKinnon, W.B., Khurana, K.K. (Eds.), Europa*. University of Arizona Press.

VAREKAMP, JOHAN C. & ROWE, GARY L. 1997 Exotic fluids in the exosphere: When hades meets apollo. *Eos, Transactions American Geophysical Union* **78** (23), 237–238.

VISBECK, MARTIN, MARSHALL, JOHN & JONES, HELEN 1996 Dynamics of isolated convective regions in the ocean. *Journal of Physical Oceanography* **26** (9), 1721 – 1734.

WARD, DANIEL ROBERT 2022 Unifying laminar and turbulent dynamics of plumes. Ph.d. thesis, University of Leeds.

YANG, JUN, PELTIER, W. RICHARD & HU, YONGYUN 2012 The initiation of modern "soft snowball" and "hard snowball" climates in ccsm3. part ii: Climate dynamic feedbacks. *Journal of Climate* **25** (8), 2737 – 2754.